

# All-Optical Computing Using the Zeno Effect

*Bryan C. Jacobs, Chad N. Weiler, Jeffrey P. Maranchi, Chad R. Sprouse,  
Dennis G. Lucarelli, and Brian G. Rayburn*

**A**ll-optical switching and logic elements could be at the forefront of next-generation computing and telecommunications systems, but only if a few key issues with the technology can be resolved. We have developed an approach based on the Zeno effect that could overcome two of the biggest challenges with this technology: the need for intense optical fields and excessive power dissipation. A key feature of our approach is the somewhat counterintuitive use of optical absorption to implement an ultra-low-loss switch. In this article, we summarize the fundamental principles of our approach and present promising theoretical results detailing the potential performance of these devices. We also describe our experimental approach to demonstrating this technology, which includes a diverse combination of microdevice development and spectroscopy experiments in atomic vapors.

## INTRODUCTION

Although high-capacity optical communications are now commonplace, the optical signals are typically routed to their destination via an electrical switching network. Or, when the routing information is also optical, it is currently converted to electrical signals for processing. These types of interconversions are not only slow (relative to the speed of light) but also dissipate considerable energy. All-optical switching technologies, where one optical signal directly controls the path of another, could potentially enable switching and logic operations at very high speeds with extremely low power dissipation. However, the relatively weak strength of optical

nonlinearities currently requires the use of intense control (switching) fields, which greatly increase losses and tend to decrease the switching speed. Additionally, the switching performance, or contrast, of existing all-optical devices is not uniform across a signal pulse because the switching mechanism itself depends on the signal intensity. This can lead to signal degradation and limit the bandwidth of a device.

APL, in collaboration with researchers at the University of Maryland, Baltimore County, and Battelle, has been investigating the potential use of the Zeno effect (see Boxes 1 and 2) to enable novel devices for all-optical

information processing applications.<sup>1-4</sup> The cornerstone of these devices is an optical medium that has a high two-photon absorption (TPA) rate but relatively low single-photon losses (SPLs). This approach, which is sum-

marized here and described in more detail in Ref. 1, uses a high quality ( $Q$ ) factor microresonator to enable the desired performance in two distinct ways. First, the optical mode volume confinement in the resonator enhances

**BOX 1. THE QUANTUM ZENO EFFECT: A WATCHED POT DOESN'T BOIL**

The quantum Zeno effect (QZE) is one of the more intriguing aspects of quantum mechanics because it predicts that frequent measurements can essentially freeze the normal evolution of a quantum system; the watched (quantum) pot really doesn't boil! This phenomenon can be described by considering the impact that measurements can have on the time evolution of an optically driven atomic system, as shown in Fig. 1.

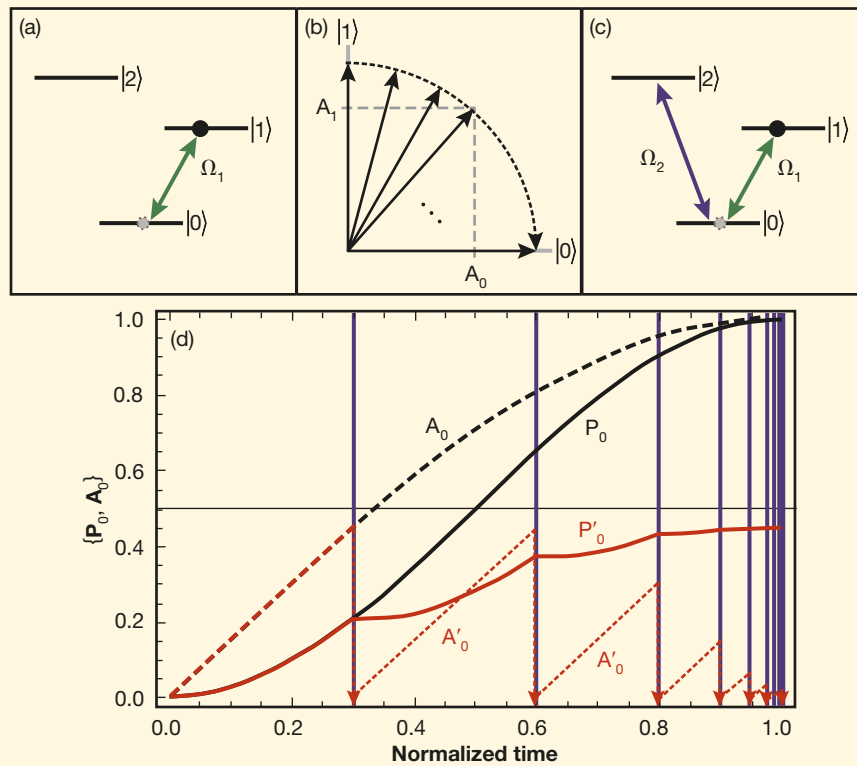


**Figure 1.** (a) *The pot:* A simple atomic system with an electron initially in the excited state,  $|1\rangle$ , and an applied optical field,  $\Omega_1$ . The field intensity and duration can be chosen to return the system to the ground state,  $|0\rangle$ , within a specified period of time, during which the system emits (*boils*) one photon. (b) The quantum state of the electron is represented by a unit vector in a complex space, and the probability ( $P_i$ ) of the electron being found in state  $|i\rangle$  is given by:  $P_i = |A_i|^2$ , where  $A_i$  is simply the projection (probability amplitude) of the state vector onto the given axis. Unobserved, the state vector continuously evolves from  $|1\rangle \rightarrow |0\rangle$  as indicated. (c) *Watching the pot:* A strong optical pulse ( $\Omega_2$ ) that only couples levels  $|0\rangle$  and  $|2\rangle$  can be used to “measure” whether the electron has transitioned to the ground state. Here we assume that these measurement pulses do not directly interact with the electron in state  $|1\rangle$ . (d) *The Zeno effect:* Unobserved, the amplitude  $A_0$  and probability  $P_0$  grow from 0 to 1 as shown. When the measurement pulses (denoted by purple stripes) are applied, the quantum state is measured and found to be in the ground state—or not. For null results, the state vector is reset to  $|1\rangle$ , meaning that  $A'_0$  (dashed red curve) is reset to 0, and the evolution pictured in panel b begins anew. In the presence of these measurements, the transition (*boiling*) time is increased because the cumulative ground state probability,  $P'_0$  (solid red curve), grows at a lower rate after each measurement. This can be seen to essentially freeze the state evolution as the measurements become continuous.

**Key Features:** The transition statistics are governed by the coherent buildup of probability amplitude into the ground state. The measurement process destroys this coherence and can essentially freeze the evolution of the quantum state. A counter-intuitive aspect of this phenomenon is that the stronger (and more frequent) the measurement process is, the less likely it is that a measurement (transition from  $|0\rangle \rightarrow |2\rangle$ ) will actually occur. This effect has been used to increase the transition lifetime in an atomic system from 1  $\mu\text{s}$  to more than 3 ms.

the nonlinearity relative to the SPL. Second, the resonant geometry and governing wave equations allow the Zeno effect to prevent multiple resonant signals from simultaneously building up in the resonator. The resulting device performance is somewhat counterintuitive because a strong TPA medium is required, but minimal energy is actually lost via TPA because of the Zeno effect.

A significant feature of our basic design is that the envisioned devices could be cascaded on a single optical chip—potentially allowing scalable, all-optical information-processing networks. This cascading feature could also enable efficient signal regeneration and control signal energy recapture, allowing the overall system dissipation to be very low. Existing all-optical devices lack this type of gate fan-out, severely limiting their practicality.

The main technical challenge to implementing our approach is achieving a sufficiently high TPA rate while minimizing SPLs. A detailed analysis<sup>1,2</sup> indicates that by using an atomic vapor as the TPA material, devices based on this approach could perform all-optical switching, logic, and memory functions with extremely low power dissipation. This will require the fabrication and resonant tuning of very-high- $Q$  resonators with sub-micrometer features, as well as developing a precise (and stable) waveguide–resonator coupling system.

Because this work grew out of our earlier quantum computing research, we begin with a brief description of this technology, focusing on TPA and the quantum and classical Zeno effects. We follow this device evolution with a brief description of three distinct types of device simulations and present theoretical performance estimates. We conclude with an overview of our current experimental approach to demonstrating this technology, which includes a diverse combination of micro-device developments and spectroscopy experiments in atomic vapors.

## FROM QUANTUM LOGIC GATES TO CLASSICAL DEVICES

### Linear Waveguide Devices

We have previously shown that TPA and the QZE can be used to implement quantum logic gates for quantum computing applications.<sup>3,4</sup> In the QZE (Box 1), frequent measurements of a quantum system can essentially prevent unwanted interactions or events from occurring. In our original quantum logic designs, a TPA material is placed between two coupled optical waveguides, as shown in Fig. 2a. Here, the input is assumed to contain at most one photon in each mode, with the photons being identical in frequency. Through detailed calculations, we showed that this device could implement a useful quantum logic operation if the Zeno effect (TPA) were strong enough to prevent two photons from occu-

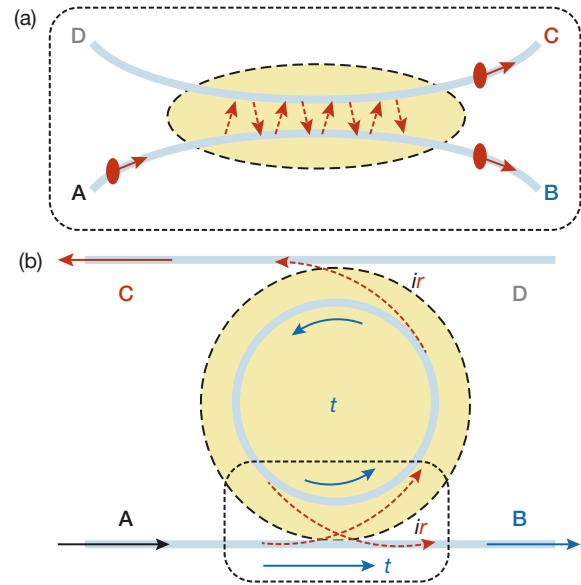


**Figure 2.** Device progression from quantum logic gates (a) to classical switches (b), where  $r$  and  $t$  are the optical mode field coupling reflection and transmission coefficients, respectively, for a lossless system  $r^2 + t^2 = 1$ . In the quantum gate, where the signal and control photons are identical, degenerate TPA (yellow cloud) is introduced along the region coupling the inputs. In the classical gate, nondegenerate TPA is used throughout a resonant ring. Corresponding input and output waveguides are labeled (A, B, C, D) for comparison purposes.

pying the same optical mode, which would correspond to an error. Unfortunately, at single-photon intensity levels, the required TPA rate is several orders of magnitude higher than is currently obtainable, making this type of geometry impracticable for the near future.

### Resonator-Based Devices

A well-known technique for enhancing optical nonlinearities is to confine the incident energy into a small volume, thereby increasing the field intensity and nonlinear effects. A common way to implement this is through the use of a ring resonator, as shown in Fig. 2b. For quantum logic operations, one photon could be switched into the ring and then the lower coupling region (dotted box) roughly corresponds to the linear waveguide device shown in Fig. 2a. We have investigated the potential effectiveness of several device geometries assuming demonstrated resonator and TPA material characteristics; unfortunately, the effective nonlinear enhancement is still insufficient for logic operations at the single-photon level.

Shortly after our initial work, we realized that it may be possible to use these same effects at higher intensity levels (i.e., with classical light sources) as long as the inputs are at different wavelengths and the absorption is tuned accordingly; i.e., we utilize nondegenerate TPA. The motivations for considering this type of operation

are to reduce the TPA requirements by moving to sufficiently high input intensities and to increase the potential range of applications to include classical switching and computing. As with the quantum case, if the TPA is strong relative to the mode coupling, then the QZE should prevent all photons from coupling (switching) into the opposite mode when both signals are present. In the *Quantum Density Matrix Analysis* section, we present the results of a quantum analysis of this type of system, which again indicates that demonstrated TPA materials are insufficient to achieve the desired operation using the QZE alone.

### Normal Resonant Operation

Although the QZE does not significantly enhance the operation of the ring resonator device pictured in Fig. 2b, a complete analysis of the device operation revealed that sufficient TPA distributed along the ring

could enable a new class of device based on a classical equivalent of the QZE. It is well known that a ring resonator coupled to two waveguides can be used to implement an optical switch by simply controlling the resonant frequency of the ring, via thermal expansion, for example. When an incident signal in one mode (A) is off resonance with the ring, most of the energy will be transmitted past the ring and exit in the output waveguide mode (B); we will refer to this as *forward scattering* or *transmission*. However, on resonance, constructive interference causes the energy within the ring to grow while destructive interference causes the forward-scattered signal to diminish (see Fig. 3 in Box 2). Eventually, the transmitted signal is negligible and the signal energy is reflected out of the ring through the other waveguide (C). Although switches are made in this manner, it is difficult to change the resonant condition quickly ( $<1$  ms) with thermal or mechanical controls.

### BOX 2. RING RESONATORS AND THE CLASSICAL ZENO EFFECT

The classical version of the Zeno effect mirrors the quantum effect shown in Box 1 in many respects; however, it can be understood using Maxwell's equations to describe the time-dependent evolution of an electromagnetic field in a resonant system.

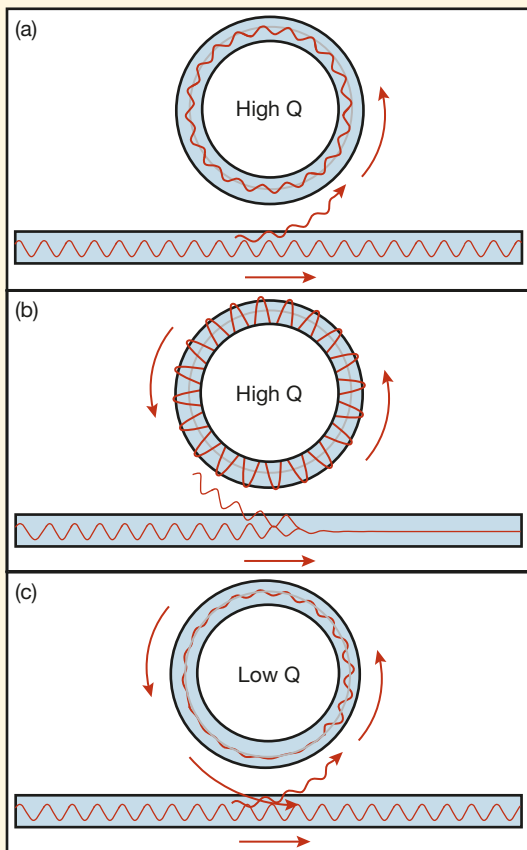


**Figure 3.** (a) *The pot*: The system considered here consists of an optical waveguide weakly coupled to an ultra-high-Q ring resonator—i.e., the ring has an ultralow optical loss coefficient. The weak coupling only permits a small fraction ( $r = 0.095$ ) of the incident electromagnetic field amplitude (red) into the ring. (b) Although the coupling is weak, the low loss in the ring allows the internal field to build up coherently for resonant input fields—i.e., when the ring circumference is an integer number of optical wavelengths. Additionally, on resonance, any light coupled out of the resonator back into the waveguide is  $180^\circ$  out of phase with the input, resulting in destructive interference. If the coupling is carefully chosen to match the loss in the resonator, then the destructive interference can extinguish the forward-going field; in this situation, the ring is dissipating exactly the same amount of energy flowing into the system. (c) *Watching the pot*: If the losses in the ring can be increased (e.g., via the application of another field and an optical nonlinearity—see the text), then the weakly coupled incident field can be dissipated in less than one loop around the ring. Now there is no significant field to couple back into the waveguide, and the majority ( $t = 0.995$ ) of the field propagates past the resonator.

**Key Features:** On resonance, the effective transmission past the resonator is governed by the coherent buildup of electromagnetic field amplitude in the ring. Increased loss (dissipation) in the ring makes the resonant condition irrelevant, and no coherent interference effects are observed. A counterintuitive aspect of this phenomenon is that higher losses in the ring lead to lower overall energy loss because very little field energy is actually coupled into the ring!

## Resonant Operation with TPA

Now consider the operation of the same device (Fig. 2b) assuming that strong TPA can occur along the ring. If only one field (the signal) is input, then the TPA is irrelevant (see Box 3), and the resonant interference effects cause the signal to be reflected from the device as described above. However, if another optical field (the control) is present in the ring, then nondegenerate TPA will occur where the control and signal fields overlap. If this absorption is strong enough, photons entering the ring will be strongly attenuated and the signal field will not grow inside the ring. Without a strong resonator field to couple back into the initial waveguide, there will be no destructive interference of the forward mode. Thus, with the control field present in the ring, the resonance condition is irrelevant and the signal will be transmitted (switched) past the resonator.

In addition to functioning as an optically controlled switch, this same structure can be seen to implement a memory because either field can act as the control and dominate the ring. For equal-intensity inputs, the dominant field will simply be the one applied first (hysteresis), and the state of the device can be flipped by briefly lowering the controlling field. One of the interesting scientific results of this investigation is that there appears to be a classical analog of the QZE; i.e., using just classical electromagnetic concepts, these devices can be seen to exhibit the same type of state-freezing behavior as a quantum system subject to frequent measurements.

## DEVICE SIMULATIONS

The feasibility of the device concept described above was investigated using a combination of classical, semi-classical, and quantum analysis techniques. Three distinct types of analysis were performed in order to explore the operation of these devices in different limits and to build up confidence in the overall result. One of the reasons for the diversity in analysis tools stems from the nature of the problem: utilizing quantum effects for classical signals. Several quantum calculations were required to develop the fundamental physics; however, remaining in the quantum realm at large (classical) field

levels was impractical for the majority of the device performance analysis. Wherever models overlapped (or could be made to overlap), numerical comparisons were performed and the results were consistent.

## Finite-Difference Time-Domain Simulations

The Finite-Difference Time-Domain (FDTD) method was used to perform high-fidelity numerical simulations of the two-dimensional optical switch shown in Fig. 2b. As the name implies, FDTD<sup>5</sup> calculates electromagnetic field values by using finite difference approximations to all spatial and temporal derivatives in Maxwell's curl equations:

$$\epsilon \partial_t \mathbf{E} = \nabla \times \mathbf{H} - \sigma \mathbf{E}, \quad (1)$$

$$\mu \partial_t \mathbf{H} = -\nabla \times \mathbf{E}. \quad (2)$$

The electric ( $\mathbf{E}$ ) and magnetic ( $\mathbf{H}$ ) fields are propagated (stepped) in time by amounts determined by the spatial variation of the other field.

For many problems it is a good approximation to assume that Maxwell's equations are linear, meaning that the material properties do not depend on the field strengths. However, the TPA mechanism considered here is a nonlinear effect that can be incorporated into the FDTD method by allowing the conductivity  $\sigma$  in Eq. 1 to depend on the field intensity  $I = |\mathbf{E} \times \mathbf{H}|$  according to

$$\sigma = \gamma I \sqrt{\frac{\epsilon}{\mu} + \left(\frac{\gamma I}{2\mu\omega}\right)^2}. \quad (3)$$

This dependence results in a loss mechanism that increases with increasing intensity. The optical switch exploits this loss by tuning the wavelength of two beams, referred to as the *control* and *signal* beams, such that one photon from each beam can be absorbed as a pair. To simulate this effect, the conductivity encountered by the signal beam should depend on the intensity of the control field but not on the intensity of the signal itself. This was accomplished by running separate control and signal FDTD simulations in tandem, using the field intensities from one to modify the material parameters of the other

### BOX 3. TWO-PHOTON ABSORPTION

Linear absorption of light occurs in a medium when the energy of the incident photons corresponds to the energy required to excite an electron to a higher energy level; one photon  $\rightarrow$  one electronic excitation. TPA is a nonlinear process wherein two incident photons are simultaneously absorbed by one atom; two photons  $\rightarrow$  one excitation. For TPA to occur, the combined photon energies must correspond to an allowed single-photon absorption energy. Because photon energies are proportional to their optical

frequency, TPA can generally occur only if the sum of the incident frequencies corresponds to a single photon transition. Accordingly, the frequencies of the two photons may be equal (degenerate) or different (nondegenerate). Degenerate TPA is used for quantum logic devices where the photonic qubits must be indistinguishable. Nondegenerate TPA is required in the classical Zeno devices because, in these devices, each logical signal contains many identical photons—otherwise, a signal would extinguish itself.

at each time step. For example, the first simulation calculates the signal field with the conductivity defined by Eq. 3, where  $I = I_c$  is the intensity of the control obtained from the second simulation. When the control field is off, this intensity, and hence the conductivity, is zero.

Figure 4 shows the results of the simulation with the control off (a) and on (b). In both cases, only the signal field is displayed, and it is introduced in the lower-left port as a sinusoidally driven field. When this signal reaches the junction with the central resonator, a small fraction ( $r = 0.095$ ) of the field amplitude is coupled (reflected) into the cavity, and the majority ( $t = 0.995$ ) is nominally transmitted past the resonator; note that these coupling coefficients ( $t$  and  $r$ ) correspond to a lossless beam splitter, i.e.,  $t^2 + r^2 = 1$ .

Intuitively, with such small coupling we would expect more than 99% ( $t^2$ ) of the incident energy to be transmitted past the ring; however, with the control off, most of the energy of the signal eventually couples into the ring because of resonant interference effects (see Box 2) and leaves the domain through the upper-left port. This can be seen in the quasi-steady state field distribution shown in Fig. 4a. But, with the control field on, non-degenerate TPA makes the resonator path highly lossy for the signal field, and consequently, the majority of the energy remains in the lower waveguide. This switching behavior can be seen in Fig. 4b.

The simulation domain shown in Fig. 4 measured  $50 \times 35$  nm at a resolution of 25 nm. Each run consisted of 6 million time steps for a total simulation time of 0.25 ns, which took approximately 1 week of run time on an eight-core Linux workstation. The FDTD method provided the ideal means for modeling the nonlinear behavior of the TPA optical switch. Creating our own code allowed us the flexibility to run two simultaneous, mutually interacting simulations. This novel approach provided a relatively quick and efficient way to simulate the switching performance without requiring a significant software/modeling development effort.

## Dynamic Device Simulations

Although the FDTD simulations provide a rigorous baseline for potential device performance, the required run time is prohibitive for device parameter optimization studies. Additionally, when the incident fields are on resonance with the ring, we can calculate approximate field values at discrete times very efficiently. Here we generate discrete input fields at a rate corresponding to one-half of the ring propagation time. Then, standard coupling and propagation equations (including loss and TPA terms) are used to calculate the fields in the linear waveguides and around the ring in half-step intervals; our only approximation is the use of average field values within the ring to calculate the nonlinear losses.

The input and retarded resonator fields are combined at the coupling regions, using the appropriate transmission and reflection coefficients, to generate the output field values. This technique permits us to quickly estimate the dynamic response of the system to pulsed inputs under a variety of conditions (e.g., resonator quality factors, coupling coefficients, TPA strength, etc.). In fact, the device parameters for the FDTD simulations described above (such as the coupling coefficients) were chosen based on the results of these dynamic simulations. This also allows us to explore the temporal response of these devices in various switching and memory scenarios. A typical switching result is shown in Fig. 5, where a  $25\text{-}\mu\text{W}$  control signal is used to switch a 500-ps pulse with the same peak intensity.

## Quantum Density Matrix Analysis

Numerical simulations of the quantum master equation (see Box 4) modeling linear loss and continuous TPA were performed to quantify the quantum Zeno behavior of the system. Here we briefly describe the model and present simulation results showing the impact the QZE has on the system. For this analysis we are only interested in quantum effects in the coupling region

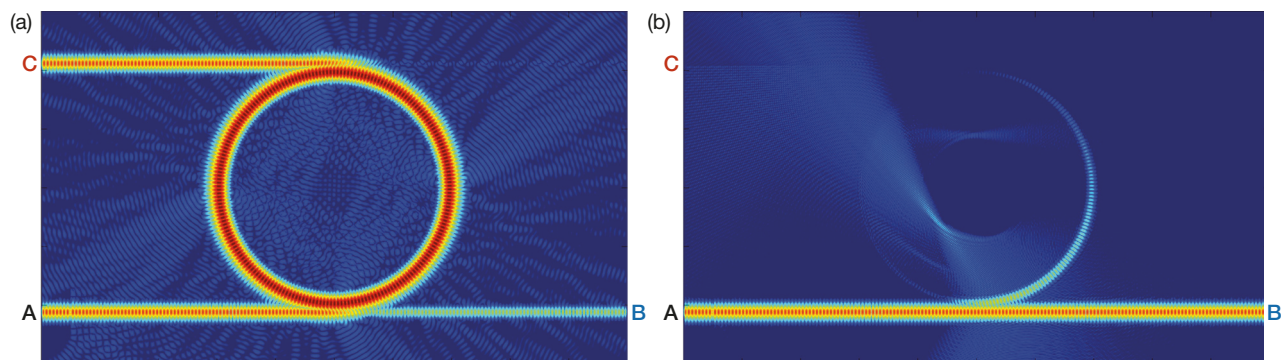


**Figure 4.** Numerical simulation of the optical switch with the control off (a) and on (b). In both panels, the source enters the switch from the lower left (mode A), and the control field is not shown in either panel. With the control off, the intensity in the resonator grows and the signal exits at the upper left (C). With the control-on energy entering, the ring is dissipated and the signal exits the lower right. Color scale is relative intensity in decibels.

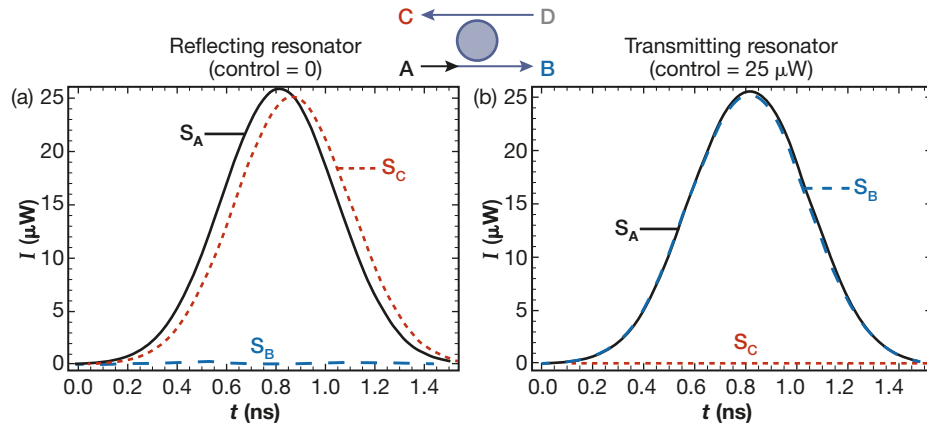


**Figure 5.** Dynamic simulation result showing low-loss optical switching. (a) With the control off, the output signal ( $S_C$ ) is a slightly delayed and attenuated version of the input,  $S_A$ ; (b) with the control on, the output signal ( $S_B$ ) follows the input with very little loss. These results highlight the counterintuitive nature of the Zeno effect, because the losses when TPA can occur (control on) are actually less than when it cannot.

between the primary waveguide and the resonator—i.e., the dotted box in Fig. 2.

The equation modeling the coupling and loss mechanisms was derived from the standard operator expressions for single- and two-photon loss by forming a Lindblad equation with an interaction Hamiltonian given by evanescent coupling between the modes. Using the number (Fock) state basis, a matrix representation was obtained and a linear ordinary differential equation was instantiated for the time evolution of the corresponding density matrix. The dimension of this system grows rapidly with respect to the number of photons modeled. For example, a system with only 10 signal photons requires the solutions of ~40,000 ordinary differential equations.

To obtain a tractable computational problem, the control field was assumed to be constant within the resonator and not explicitly modeled in the differential equations; however, its effect by means of TPA on the signal field was retained. This was achieved by including the photon number states for the signal field in both

optical modes and capturing the TPA by an appropriately scaled loss rate. The basic model was cross-checked with the dynamic simulation results by comparing the TPA rates when both photons were freely propagating in the same mode; in this case, there was no QZE because the mode coupling was turned off. The model was also checked by running the simulation with the loss terms disabled. The result, which is shown in Fig. 6a, shows the expected transfer of all photons into the resonator mode after a given coupling length. This result

was also used to set the baseline coupling strength to correspond to a transmission coefficient of  $t = 0.995$ .

A series of simulations were performed to assess the operation of the switch while varying the TPA coefficient. For each value of TPA, the four-mode system was integrated with the signal coupling coefficient set as for the simulation in Fig. 6a. The results are plotted in Fig. 6b, demonstrating an increase in expected transmission probability as the cross-TPA strength is increased. This indicates that for sufficiently high TPA, the QZE will enhance the operation of the gate and lead to even lower losses.

### EXPERIMENTAL OVERVIEW AND DEVICE DESIGN

A device concept for a Zeno effect optical switch that could potentially be integrated into a single substrate and mass produced is shown in Fig. 7a. It consists of two curved waveguides proximate to a ring resonator surrounded by an atomic vapor. The envisioned device

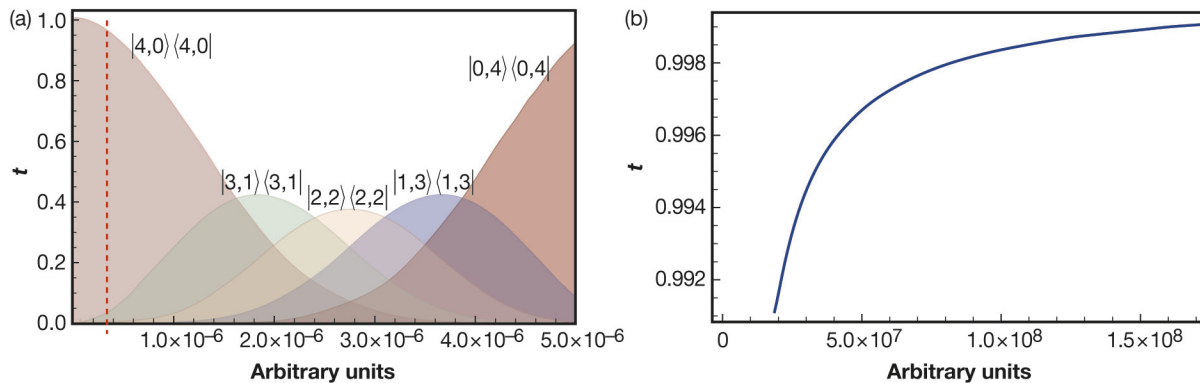


**Figure 6.** (a) Trajectories of the diagonal elements of the density matrix of the system with the control off. The dashed line indicates coupling strength at which  $t = 0.995$ . (b) Transmission coefficient as the TPA strength is increased.

**BOX 4. THE MASTER EQUATION**

The Schrödinger formulation of quantum mechanics describes the evolution of a state vector that completely characterizes the quantum dynamics for systems that are well isolated from the environment. Modeling SPL and TPA requires a generalized version of the state vector, known as the density matrix. In “ket” notation, let  $\{|\psi_a\rangle, a = 1, \dots, n\}$  denote a basis for the underlying finite dimensional vector space of the quantum system. A density matrix represents a statistical mixture of states as

$$\rho = \sum_a p_a |\psi_a\rangle\langle\psi_a|, \quad (\text{B1})$$

where the operator  $|\psi_a\rangle\langle\psi_a|$  is simply a matrix and the coefficients  $p_a$  sum to one. The probabilistic nature of quantum mechanics is reflected in the interpretation of a diagonal element of the density matrix  $\rho_{bb}$  as the average probability of finding the system in the state  $|\psi_b\rangle$ . Without environmental interactions (loss), the time evolution of the density matrix is governed by

$$\frac{d\rho}{dt} = -i[H, \rho] = -i(H\rho - \rho H), \quad (\text{B2})$$

where  $H$  is the Hamiltonian operator that describes couplings between states, or optical modes in our problem. When a set of linear operators ( $L_k$ ) is used to model optical losses (TPA), the density matrix evolves according to the Lindblad master equation:

$$\frac{d\rho}{dt} = -i[H, \rho] + \sum_k \lambda_k (2L_k \rho L_k^\dagger - L_k^\dagger \rho - \rho L_k^\dagger L_k), \quad (\text{B3})$$

where the  $\lambda_k$  parameterize the strength of the interactions.

Because we are interested in tracking the propagation of photons throughout our system, we will use the Fock state basis, where a ket  $|n\rangle$  represents an optical mode containing  $n$  photons. We will also use the standard photon *creation* and *annihilation* operators  $a^\dagger$  and  $a$  that are defined by their action on Fock states as

$$a^\dagger |n\rangle = \sqrt{n+1} |n+1\rangle, a |n\rangle = \sqrt{n} |n-1\rangle. \quad (\text{B4})$$

In this notation, the coupling between optical modes is represented by operator pairs  $\sim a_2^\dagger a_1$  in the Hamiltonian, which reflect the quantization of the electromagnetic field and conservation of photon number as energy is moved, from mode 1 to mode 2 in this case.

Here we are only interested in modeling interactions between the lower waveguide (A) and resonator (R) shown in Fig. 1; however, because the signal (S) and control (C) photons have different frequencies, this requires a state vector with four modes,  $|n_1 n_2 n_3 n_4\rangle \Leftrightarrow |A_s R_s A_c R_c\rangle$ . For clarity, the operator  $a_3$  annihilates a control photon in waveguide A. Neglecting SPL, the master equation modeling the evolution of the density matrix is given by

$$\frac{d\rho}{dt} = i[(H_s + H_c), \rho] + \alpha \left( \underbrace{2a_1 a_3 \rho a_3^\dagger a_1^\dagger - a_3^\dagger a_1^\dagger a_1 a_3 \rho - \rho a_3^\dagger a_1^\dagger a_1 a_3}_{\text{crossTPA mode A}} + \underbrace{2a_2 a_4 \rho a_4^\dagger a_2^\dagger - a_4^\dagger a_2^\dagger a_2 a_4 \rho - \rho a_4^\dagger a_2^\dagger a_2 a_4}_{\text{crossTPA mode B}} \right), \quad (\text{B5})$$

where  $H_s = \epsilon_s (a_1^\dagger a_2 + a_1 a_2^\dagger)$  and  $H_c = \epsilon_c (a_3 a_4 + a_3 a_4)$  are the Hamiltonians describing the coupling for each frequency mode with coupling strength  $\epsilon$ , and  $\alpha$  denotes the TPA coefficient.

Denoting the density matrix of the joint system by

$$\rho = \sum \rho_{mnuv, pqwx} |mnuv\rangle\langle pqwx|, \quad (\text{B6})$$

a system of linear ordinary differential equations for the coefficients may be derived from the master equation.

$$\begin{aligned} \dot{\rho}_{mnuv, pqwx} = & -i\epsilon_1 (\sqrt{m(n+1)} \rho_{m-1n+1uv, pqwx} + \sqrt{n(m+1)} \rho_{m+1n-1uv, pqwx} \\ & - \sqrt{q(p+1)} \rho_{mnuv, p+1q-1wx} - \sqrt{p(q+1)} \rho_{mnuv, p-1q+1wx}) \\ & - i\epsilon_2 (\sqrt{u(v+1)} \rho_{mnu-1v+1, pqwx} + \sqrt{v(u+1)} \rho_{mnu+1v-1, pqwx} \\ & - \sqrt{x(w+1)} \rho_{mnuv, pqw+1x-1} - \sqrt{w(x+1)} \rho_{mnuv, pqw-1x+1}) \\ & + \alpha (2\sqrt{(m+1)(u+1)(p+1)(w+1)} \rho_{m+1nu+1v, p+1qw+1x} \\ & + 2\sqrt{(n+1)(v+1)(q+1)(x+1)} \rho_{mn+1uv+1, pq+1wx+1} \\ & - (mu + pw + nv + qz)) \rho_{mnuv, pqwx}. \end{aligned} \quad (\text{B7})$$

Vectorizing the density matrix and using the previous expression for the time behavior of the coefficients results in a large-scale system of linear differential equations that can be numerically integrated. Because we are primarily interested in the evolution of the signal photons, we calculate the reduced density matrix  $\rho^s$  by performing a partial trace over the control modes:

$$\rho^s \equiv \text{Tr}_c(\rho) = \sum a_{mn, pq} |mn\rangle\langle pq|, \quad (\text{B8})$$

where  $a_{mn, pq} = \sum_{uv} \rho_{mnuv, pquv}$ . Here the state space is reduced to  $|n_1 n_2\rangle \Leftrightarrow |A_s R_s\rangle$ .

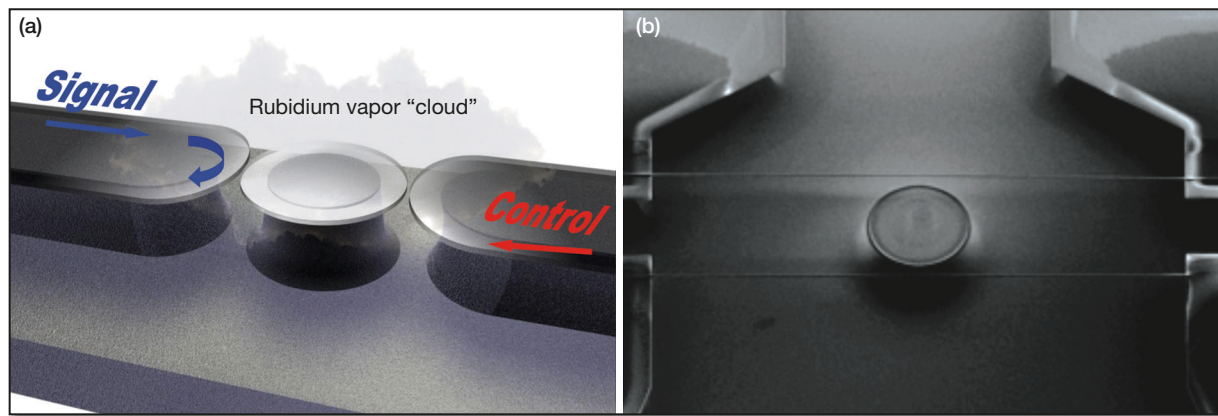


**Figure 7.** (a) Zeno effect microdevice concept, showing all features on one integrated chip. (b) Experimental Zeno switch prototype using tapered optical fibers to couple to a microtoroid.

would require substantial development because it would also need to include microelectromechanical systems-based stages to tune the couplings between the resonator and the waveguides. We are currently developing experimental prototypes that are designed to demonstrate the basic device operation without these extra complications. Although we are pursuing two different fabrication technologies, silicon oxide<sup>6</sup> and silicon nitride,<sup>7</sup> only the silicon oxide devices will be discussed here.

In the silicon oxide approach, a silica microtoroid is fabricated on a silicon wafer as described in the *Toroid Fabrication* section. Separately, tapered optical fibers<sup>8</sup> are produced via the flame brushing technique or a modified version of the flame brushing technique as described below.<sup>9,10</sup> The tapered optical fibers are optically coupled to the microtoroid (one at a time) using a nanopositioning stage and then tacked to on-chip supports using UV-curing optical resins or micrometal spot welds. A recently fabricated silica microtoroid with mounted optical fiber waveguides is shown in the scanning electron microscope image in Fig. 7b. In order to complete the device, the resonator must be surrounded

by an atomic vapor of an appropriate two-photon absorber such as rubidium alkali metal vapor. A vacuum chamber with a glass cell containing the device is being used. The alkali metal vapor is introduced to the glass cell using commercial, resistively heated alkali metal dispensers after a pumping down to a base pressure of roughly  $10^{-8}$  Torr. The vapor pressure surrounding the resonator is controlled by manipulating the temperature of the glass cell as well as by perturbing the equilibrium vapor pressure via light-induced atomic desorption (LIAD) effects, as discussed in the *Light-Induced Atomic Desorption* section.

### Toroid Fabrication

Our silicon oxide devices are fabricated through a sequence of photolithographic and etching steps as described in the literature. The result is a silica disc atop a silicon pedestal, as shown in Fig 8a. These devices can have intrinsic  $Q$  factors (or  $Q$ 's) of roughly  $10^6$  without any additional processing; however, by using a technique known as laser reflow to reshape the disc and reduce the

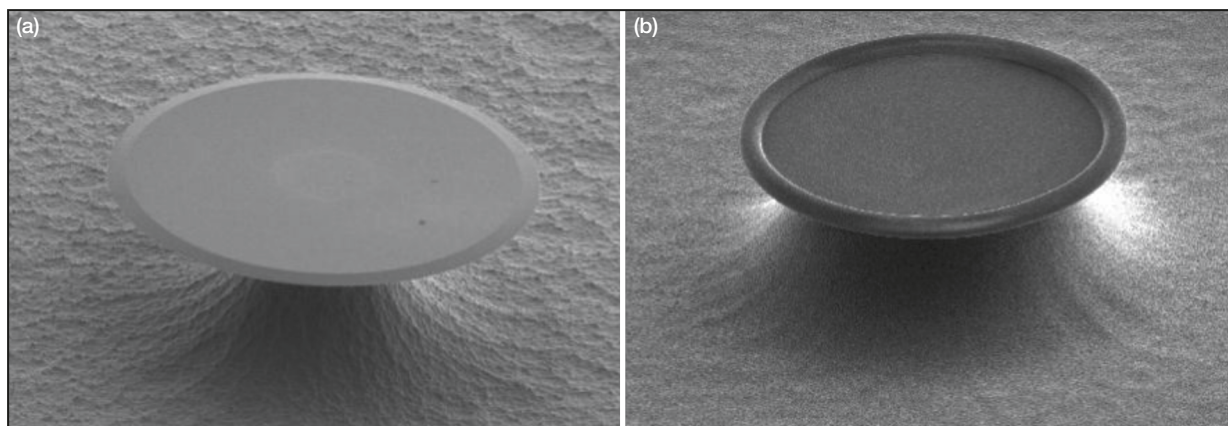


**Figure 8.** The resonant structures for the Zeno devices can be thin silica discs (a) or toroids (b). The toroids are fabricated by partially melting a disc using a  $\text{CO}_2$  laser reflow process.

surface roughness, intrinsic  $Q$ 's of  $\sim 10^8$  can be readily obtained.

Fabrication of a toroid from a disc is accomplished using intense pulses of light from a  $\text{CO}_2$  laser operating at  $10.5\ \mu\text{m}$ . Although the laser beam is delivered uniformly across the disc, the overhanging region melts first and curls up into a toroid. This is because the silicon pedestal is a much better thermal conductor than the silica disc. Thus, the silica above the pedestal remains below the melting point while the overhanging silica reaches the melting point. Surface tension drives the molten silica into its lowest energy configuration, which is a toroid. This is a self-limiting process, with the final toroid dimensions governed by the initial oxide thickness and the amount of overhang. We routinely make toroids with minor diameters of roughly  $1\ \mu\text{m}$ .

The resonators (toroids and discs) are characterized by positioning a tapered optical fiber to within a few nanometers of the resonator and examining the spectral characteristics of light transmitted through the fiber. The spatial overlap of the optical modes of the fiber and resonator govern the strength of the coupling between them. We can adjust this coupling by launching light (typically  $780\ \text{nm}$ ) into the fiber and then using a charge-coupled device camera to monitor any light scattering out of the resonator. We then measure the spectral structure of the resonator by scanning the laser wavelength over tens of nanometers and recording the intensity transmitted past the resonator. As the source wavelength moves into resonance with the device, the transmission is extinguished because of destructive interference. The largest dip (Fig. 9) represents the fundamental mode supported by the resonator. Generally speaking, multiple dips are seen because different polarizations are resonant at slightly different frequencies. Maximum resonance dips can be achieved by adjusting the polarization of the input light to isolate one of these resonances. The central wavelength ( $\lambda_0$ ) and full width at half maximum ( $\Delta\lambda$ ) of the resonance provides an estimate of the quality factor:

$$Q \cong \lambda_0 / \Delta\lambda. \quad (4)$$

### Fiber Tapering

Tapered optical fibers<sup>8</sup> are created by heating and drawing a region of silica fiber down to diameters on the

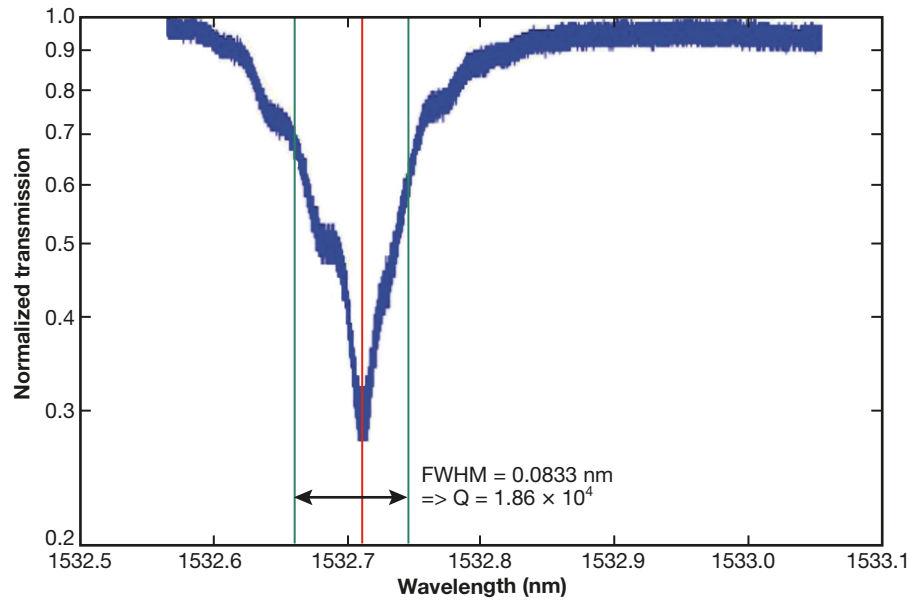


**Figure 9.** Fundamental mode resonance of a disc resonator. Typical transmission spectrum through a tapered optical fiber in contact with a ring resonator. The dip occurs when the ring diameter is an integer number of optical wavelengths. The resonance dip only drops all the way to zero if the coupling exactly matches losses in the resonator. In this case, the fiber is in contact (overcoupled) with the resonator. FWHM, full width at half maximum.

order of a micrometer. At these dimensions, the optical mode is guided by the difference in refractive index between the glass and air, creating an air-clad optical mode. Because a portion of this mode travels outside the fiber in what is called an evanescent field, access to this field is physically possible.

Typically, fiber pulling has been done by heating the fiber with a flame. The region above the softening temperature of the glass is referred to as the hot zone. The hot zone provides a source of lower-viscosity glass from which to create the taper region during the pull. By approximating the hot zone as a step function in the region where the flame is above the softening point of the glass, an exponential relationship between the pull length and the waist of the fiber can be derived. Because the hot zone length determines the rate of the exponential decrease in fiber waist, the size of the hot zone must be controlled precisely. Excellent hot zone control can be achieved by oscillating a microtip flame burner over a section of fiber, creating an effective hot zone of the desired size.

Compared with a hydrogen-fueled flame, propane and butane provide a relatively gentle flame in the right temperature range to soften the glass without melting; however, hydrocarbon combustion products have been shown to irreversibly contaminate the fiber while it is soft, creating defects that increase the optical losses and weaken the fiber. Although hydrogen flames burn cleaner than hydrocarbon fuels, the water vapor produced during combustion unfortunately creates micro-

cracks in the surface of the fiber, again limiting the usability and longevity of the tapered fiber.

The turbulence associated with a torch approach also limits the reproducibility of submicrometer fibers by complicating the mechanical forces on the fiber during taper pulling. Flame temperature fluctuations also reduce the repeatability of tapers by varying the hot zone, and as a result, the geometry of the tapered region.

To avoid the caustic and destructive effects of direct flame heating, fiber furnaces have been developed.<sup>9,10</sup> By delivering mostly radiative heat in furnaces, the mechanical forces exerted on the fiber can be reduced and the flame by-products are isolated from the softened glass. Temperature stability is also increased by having a more stable (massive) heating element in the furnace to essentially average over temporal variations in the flame temperature.

The furnace developed at APL uses a hydrogen torch to heat a molybdenum disilicate ( $\text{MoSi}_2$ ) radiator. This material is commonly used in heating elements because it has a high thermal conductivity and a low thermal expansion coefficient and can withstand temperatures up to  $1700^\circ\text{C}$ . Alumina and alumina/silica insulation and support structures surround the  $\text{MoSi}_2$  cylinder. Our furnace has a 3.5-mm hot zone when operated at a maximum temperature of  $1270^\circ\text{C}$ . The hot zone roughly corresponds with the length of the furnace above  $1170^\circ\text{C}$ , which is the softening point of our silica fibers (Corning SMF-28). The furnace temperature is monitored by a reference thermocouple embedded in the ceramic foam. Although we have produced usable tapers with diameters less than 450 nm using this setup (Fig. 10), additional refinements are needed to decrease the diameter further and improve our process control.

## Two-Photon Absorption

The potential performance of the Zeno effect switches described above requires a medium with very strong, nondegenerate TPA but relatively low SPL; i.e., two single-frequency beams must individually pass through the medium with little or no attenuation. Isolated atomic systems are ideal for this type of application because they can have inherently narrow absorption line widths relative to solid-state systems. Furthermore, alkali metals (such as rubidium) are easily manipulated by accessible laser wavelengths because they only contain a single electron in their outer shell.<sup>11</sup> For this work, we use atomic rubidium because it has multiple ground state transitions in the 760- to 780-nm range, where tunable lasers are readily available.

A simplified diagram of the relevant rubidium energy levels is depicted in Fig. 11. Rubidium has a strong ground state transition between the  $^5\text{S}_{1/2}$  and  $^5\text{P}_{3/2}$  energy levels, corresponding to strong single-photon absorption at 780.2 nm. It also supports a strong excited state transi-

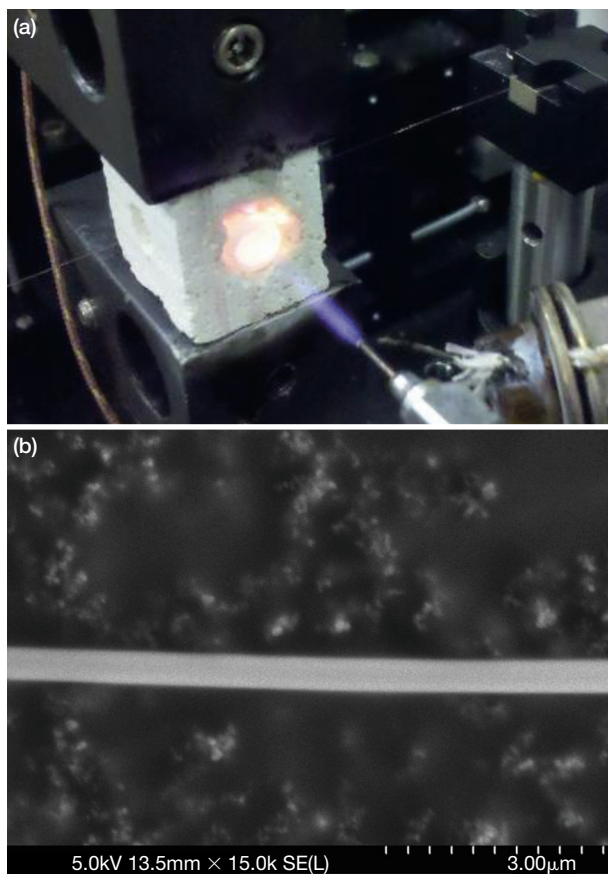


**Figure 10.** By using a homemade furnace (a) and motorized micrometers, we can pull tapered fibers with minimum diameters below  $1\ \mu\text{m}$  (b).

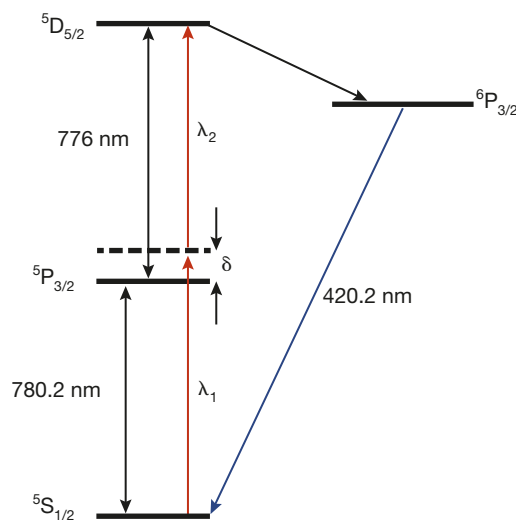


**Figure 11.** A TPA transition in rubidium is excited by tuning two independent laser wavelengths,  $\lambda_1$  and  $\lambda_2$ , such that the sum of their energies equals the  $^5\text{S}_{1/2}$ -to- $^5\text{D}_{5/2}$  transition energy. The strength of TPA is highly dependent on the detuning ( $\delta$ ) of  $\lambda_1$  with respect to the  $^5\text{S}_{1/2}$ -to- $^5\text{P}_{3/2}$  transition. The TPA condition can be easily confirmed by observing the UV fluorescence signal produced as the excited state decays via the  $^6\text{P}_{3/2}$ -to- $^5\text{S}_{1/2}$  transition.

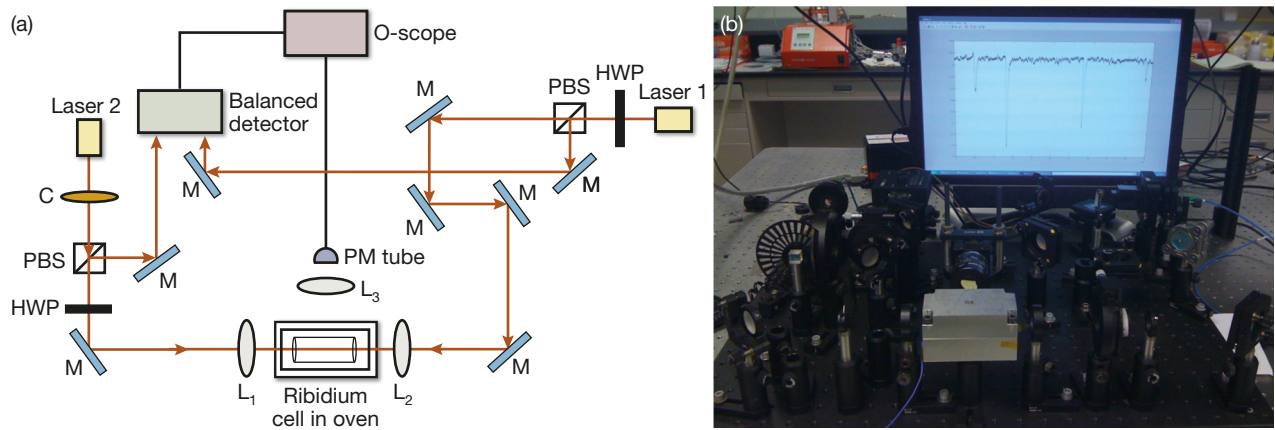


**Figure 12.** (a) Diagram of TPA setup. C, chopper; HWP, half-wave plate; M, mirror;  $L_1$ ,  $L_2$ , lens  $f = 60$  mm;  $L_3$ , lens  $f = 40$  mm; O-scope, oscilloscope; PM tube, photo-multiplier tube. (b) Actual TPA setup.

tion to the  $^5D_{3/2}$  state when both 780.2-nm and 776-nm light are present. Although this combination supports nondegenerate TPA, a single input beam at 780.2 nm would experience considerable SPL due to resonance with the ground state transition.

An interesting feature of quantum optics is that TPA can occur even if the incident photons are not exactly on resonance with the underlying transitions; the main requirement is that the combined photon energy equal the overall atomic transition energy. Consequently, if the incident fields are slightly shifted (or detuned) from the single-photon resonances, as shown in Fig. 11, then the system still supports TPA but neither input is absorbed alone. Unfortunately, the rate of TPA is strongly dependent on this detuning ( $\delta$ ) from the single-photon transition. The goal then is to choose  $\delta$  such that the rate of TPA is high while the rate of single-photon absorption remains relatively low. We have shown<sup>1</sup> that  $\delta$  should be on the order of 0.05 nm for maximal switching efficiency.

Figure 11 also shows that the excited atom can relax to its ground state through a cascade from the  $^5D_{3/2}$  state to the  $^6P_{3/2}$  state. The signature of this process is a fluorescence signal at a wavelength of 420 nm. As described below, this fluorescence signal is important in detecting the presence of TPA.

A TPA apparatus was developed to provide the necessary feedback for tuning the lasers to the correct wavelengths. A depiction of the optical setup used for our investigation is shown in Fig. 12. Two frequency-stabilized external cavity diode laser systems are used to provide (tunable) light at wavelengths  $\lambda_1 = 780.164$  nm and  $\lambda_2 = 776.057$  nm, respectively. Laser 1 is sent through a half-wave plate followed by a polarizing beam splitter (PBS). The half-wave plate is set such that a small portion of the light is reflected from the PBS and used as a reference signal for a balanced detection scheme. The portion of the beam that is transmitted is sent through a

lens whose focal point resides at the center of a rubidium spectroscopic cell (Triad Technology Inc.). Upon exiting the cell, the beam is recollimated by a second lens. The polarization of the beam is then rotated by another half-wave plate to ensure that all of the light is reflected off a second PBS and sent to the second half of the balanced detector.

Laser 2 is modulated by an optical chopper and passes through a PBS. The paths of the two lasers are set such that they are completely counter-propagating as they traverse the rubidium cell. This ensures that the detected TPA spectrum is not Doppler broadened.<sup>11</sup> For these experiments, the laser power of both beams was set to 1 mW, measured just before the spectroscopic cell. Because the TPA strength is highly dependent on the rubidium density, we adjusted the density to the desired strength by raising the temperature of the cell to  $\sim 100^\circ\text{C}$ .

A two-pronged detection scheme is used to detect the TPA spectra. Our first method collects the fluorescence signal using a double-convex lens. This signal is sent through a 10-nm-wide bandpass filter centered at 420 nm and is detected by photo-multiplier tube. The fluorescence signal is well suited for diagnosing the presence of TPA but is not easily usable for quantifying the strength of TPA. This is because self-absorption of the spontaneously emitted light can occur when TPA is strong.

In addition to the fluorescence measurement, a balanced detection scheme is implemented using a commercial balanced detector (ThorLabs PDB150). This method directly quantifies the power lost to TPA by measuring a difference signal. As stated earlier, the light from laser 1 is split such that one of the beams is used as a reference signal while the second is sent to the experiment. A well-matched pair of photodiodes in the PDB150 independently detects both signals. The photodiode signals are sent to a low-noise, variable-gain transimpedance amplifier that generates an output proportional to the difference between the two detected signals. Utilizing

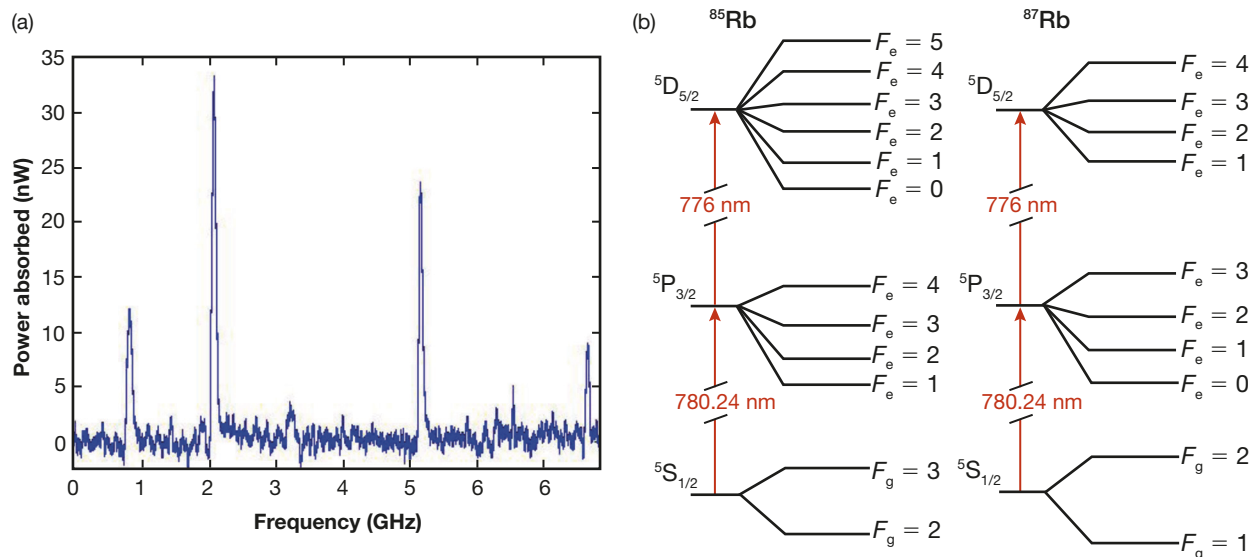


**Figure 13.** (a) TPA spectroscopic data acquired by sweeping the frequency of laser 2 with respect to laser 1. The four peaks correspond to the rubidium ground-state hyperfine levels, which can be seen in the energy level diagram (b).

the modulated signal from laser 2, further noise reduction is accomplished by sending the output of the balanced detector to a lock-in amplifier.

Spectroscopic measurements are recorded by holding laser 1’s frequency fixed while scanning that of laser 2. A scan result can be seen in Fig. 13a. The four peaks correspond to the ground state hyperfine levels<sup>12,13</sup> for the naturally occurring isotopes of rubidium, <sup>85</sup>Rb and <sup>87</sup>Rb (see Fig. 13b). As can be seen in Fig. 13b, we have been able to measure signal levels corresponding to power differences of less than 10 nW (out of a 1-mW input) for the <sup>87</sup>Rb  $F = 1$  line. The current setup is being transitioned to function as a laser lock to provide the ability to lock the lasers to the TPA line. Having the lasers tuned to the correct frequencies for maximal TPA is imperative for proper operation of the switch. The device resonance will then be thermally tuned to match the laser frequencies such that all resonances of the system will occur at the two relevant laser frequencies.

**Light-Induced Atomic Desorption**

The baseline design for the APL Zeno all-optical switching device calls for an atomic vapor of rubidium atoms with a density of more than  $5 \times 10^{10}$  atoms per  $\text{cm}^3$ . One method to alter the atomic vapor density (i.e., the number density of atoms per cubic centimeter in the vapor) is to change the temperature of the system. However, higher temperatures can potentially lead to deleterious issues with the alkali metal doping the silica glass utilized in the microtoroids and optical fibers. The addition of an alkali metal such as rubidium to a glass changes the composition of the glass and can lead to a change in refractive index, which could lead to undesirable changes in the switching performance of the device

as a function of time. It would be highly desirable to be able to temporarily increase the atomic vapor density at room temperature so that no thermal energy needs to be applied. A nonthermal approach to adjust alkali metal vapor pressure, known as LIAD, is currently being pursued at APL.

LIAD<sup>14</sup> is affected by at least two different physical phenomena, one being similar to the photoelectric effect and the other related to surface plasmon resonance, as shown in Fig. 14. In the case of isolated rubidium (metal) atoms adsorbed on a surface (adatoms), exposure to UV, or high-energy visible light, adds energy to the metal

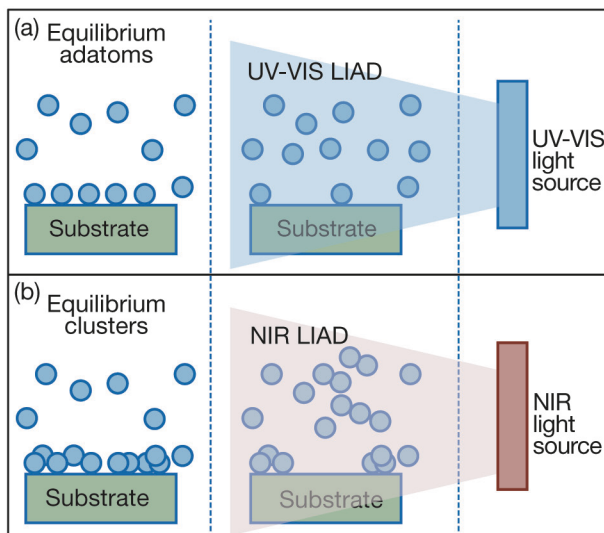


**Figure 14.** Illustration of LIAD in the case of UV-visible spectroscopy (VIS)-stimulated desorption of adatoms on a surface (a) and near infrared (NIR)-stimulated surface plasmon-based desorption of cluster atoms on a surface (b).

atoms. If the energy is sufficient to shift the adsorption-desorption dynamic equilibrium toward desorption, then the metal atom is ejected from the surface with a kinetic energy that is related to the difference between the incident photon energy and the work function of the metal atom. This process is described by the photoelectric effect:

$$E_{\text{kinetic}} = h\nu - \phi, \quad (5)$$

where  $E_{\text{kinetic}}$  is the maximum kinetic energy of the ejected atom,  $h$  is Planck's constant,  $\nu$  is the frequency of incident light, and  $\phi$  is the work function of the metal.<sup>14–16</sup> In the case of rubidium atoms, the work function is 2.16 eV, which corresponds to a maximum wavelength of light of 575 nm. Thus, UV and visible light up to wavelengths of 575 nm can be expected to be effective for LIAD of rubidium adatoms. The other phenomenon observed by researchers involves the ejection of rubidium clusters from a dielectric substrate via a surface plasmon resonance effect.<sup>17</sup>

Preliminary experiments at APL have shown significant promise toward the use of LIAD to increase atomic vapor density for the Zeno all-optical switching device. A glass test cell vacuum system has been constructed for LIAD and device testing as shown in Fig. 15. Preliminary LIAD measurements are presented in Fig. 16, which shows transmission of 780-nm light through the glass cell as a function of time. Note that rubidium atomic vapor has a strong absorption at 780 nm and that as vapor pressure increases (i.e., number density of atoms increases), the transmission will decrease. The blue curve is the noise floor of the detector. The red curve shows a significant decrease in transmission and subsequent “relaxation” back toward the equilibrium vapor pressure when a noncollimated 455-nm LED source was

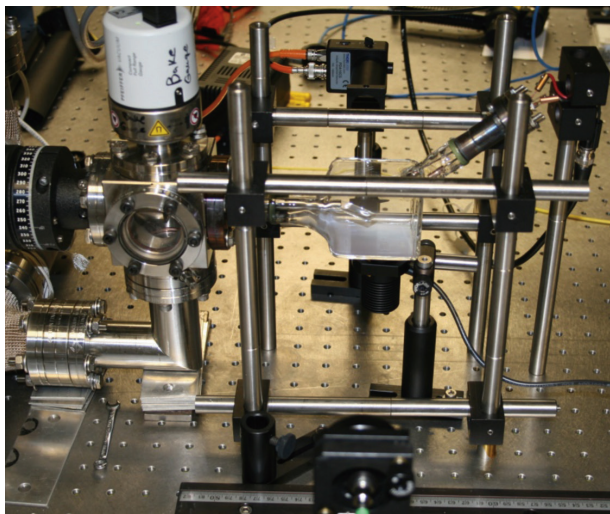


**Figure 15.** APL glass cell coated with rubidium atoms and attached to the vacuum system.

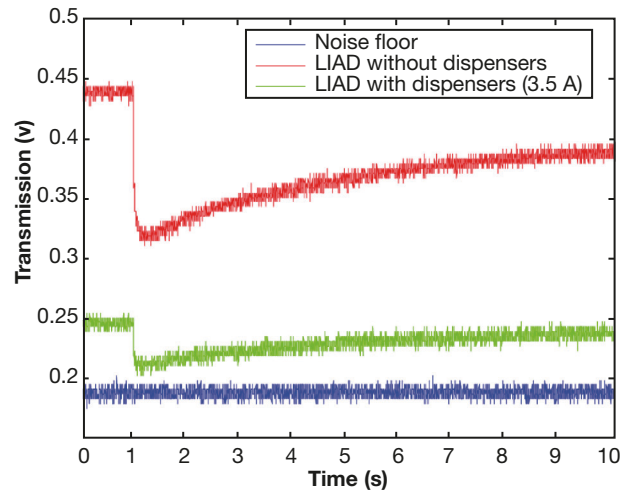


**Figure 16.** Preliminary LIAD test results showing atomic desorption decreasing transmission through the glass cell.

incident on the glass cell at a time of 1 s in Fig. 5. The green curve shows that the background vapor density can be increased even further (lower initial transmission at time between 0 and 1 s) by actively adding rubidium atoms from resistively heated alkali metal dispensers, and then at a time of 1 s, that the vapor density can be increased even further by turning on the 455-nm LED source. The photodetector signal almost reached the noise floor, indicating near-full absorption of the 780-nm light within the path length through the glass cell. The promising LIAD results indicate that further study is warranted and that implementation of LIAD in the Zeno switching device may be beneficial.

## CONCLUSIONS

Over the past few years we have developed novel approaches to photonic quantum and classical computing based on TPA and the Zeno effect. Although material and engineering demands currently place quantum logic demonstrations out of reach, we are on the verge of demonstrating a new class of device that could revolutionize conventional optical computing.

**ACKNOWLEDGMENTS:** Many of the theoretical underpinnings of this work were developed in collaboration with Dr. James Franson (University of Maryland, Baltimore County). We are also grateful to our device development collaborator, Dr. Lee Oesterling (Battelle). Finally, we acknowledge the contributions of Kevin Sobczak (master's student in the Whiting School of Engineering), who is currently automating a control system to keep the tunable lasers locked to the required TPA frequencies. The views expressed herein are those of the authors and do not reflect the official policy or position of the Department of Defense or the U.S. government.

## REFERENCES

- <sup>1</sup>Jacobs, B. C., and Franson, J. D., "All-Optical Switching Using the Quantum Zeno Effect and Two-Photon Absorption," *Phys. Rev. A* **79**, 063830 (2009).
- <sup>2</sup>Jacobs, B. C., Franson, J. D., and Oesterling, L., *Quantum Effects for Novel Optoelectronic Devices Final Report*, The Defense Advanced Research Projects Agency's (DARPA) Strategic Technology Office (STO), ARPA Order No. X032 00, Program Code 7620, Contract No. HRO011-06-D-0003-0022 (2008).
- <sup>3</sup>Franson, J. D., Jacobs, B. C., and Pittman, T. B., "Zeno Logic Gates Using Microcavities," *J. Optics B* **24**(2), 209–213 (2007).
- <sup>4</sup>Franson, J. D., Jacobs, B. C., and Pittman, T. D., "Quantum Computing Using Single Photons and the Zeno Effect," *Phys. Rev. A* **70**, 062302 (2004).
- <sup>5</sup>Taflove, A., and Hagness, S. C., *Computational Electrodynamics: The Finite-Difference Time-Domain Method*, Artech House, MA (2005).
- <sup>6</sup>Vahala, K. J., "Ultra-High-Q Toroid Microcavity on a Chip," *Nature* **421**, 925–928 (2003).
- <sup>7</sup>Barclay, P. E., Srinivasan, K., Painter, O., Lev, B., and Mabuchi, H., "Integration of Fiber-Coupled High-Q SiNx Microdisks with Atom Chips," *Appl. Phys. Lett.*, **89**(13), 131108-1–131108-3 (2006).
- <sup>8</sup>Birks, T. A., and Li, Y. W., "The Shape of Fiber Tapers," *J. Lightwave Technol.* **10**(4), 432–438 (1992).
- <sup>9</sup>Brambilla, G., Fei, X., Horak, P., Yongmin, J., Koizumi, F., et al., "Optical Fiber Nanowires and Microwires: Fabrication and Applications," *Adv. Opt. Photonics* **1**(1), 107–161 (2009).
- <sup>10</sup>Brambilla, G., Jung, Y., and Renna, F., "Optical Fiber Microwires and Nanowires Manufactured by Modified Flame Brushing Technique: Properties and Applications," *Front. Optoelectron. China* **3**(1), 1–6 (2010).
- <sup>11</sup>Jacques, V., Hingant, B., Allafort, A., Pigeard, M., and Roch, J. F., "Nonlinear Spectroscopy of Rubidium: An Undergraduate Experiment," *Euro. J. Phys.* **30**(5), 921–934 (2009).
- <sup>12</sup>Steck, D. A., *Rubidium 85 D Line Data*, Revision 2.1.4, <http://steck.us/alkalidata/rubidium85numbers.pdf> (23 Dec 2010).
- <sup>13</sup>Steck, D. A., *Rubidium 87 D Line Data*, Revision 1.6, <http://steck.us/alkalidata/rubidium87numbers.1.6.pdf> (14 Oct 2003).
- <sup>14</sup>Burchianti, A., Marinelli, C., Bogi, A., Brewer, J., Rubahn, K., et al., "Light-Induced Atomic Desorption from Porous Silica," *Europhys. Lett.* **67**(6), 983–989 (2004).
- <sup>15</sup>Karaulanov, T., Graf, M. T., English, D., Rochester, S. M., Rosen, Y. J., et al., "Controlling Atomic Vapor Density in Paraffin-Coated Cells Using Light-Induced Atomic Desorption," *Phys. Rev. A* **79**(1), 012902 (2009).
- <sup>16</sup>Klempt, C., van Zoest, T., Henninger, T., Topic, O., Rasel, E., et al., "Ultraviolet Light-Induced Atom Desorption for Large Rubidium and Potassium Magneto-optical Traps," *Phys. Rev. A* **73**(1), 13410 (2006).
- <sup>17</sup>Burchianti, A., Bogi, A., Marinelli, C., Maibohm, C., Mariotti, E., and Moi, L., "Reversible Light-Controlled Formation and Evaporation of Rubidium Clusters in Nanoporous Silica," *Phys. Rev. Lett.* **97**(15), 157404 (2006).

# The Authors



Bryan C. Jacobs



Chad N. Weiler

Jeffrey P.  
Maranchi

Chad R. Sprouse

Dennis G.  
LucarelliBrian G.  
Rayburn

**Bryan C. Jacobs** is the Principal Investigator leading the Zeno Effect Switching Technology (ZEST) research effort, which is currently funded by the Defense Advanced Research Projects Agency (DARPA). Dr. Jacobs is a Principal Professional Staff Physicist and Program Manager in the Research and Exploratory Development Department (REDD). In addition to overseeing the APL effort, Dr. Jacobs leads a collaboration in this area with researchers from University of Maryland, Baltimore County; Battelle; and Sandia National Laboratories. Dr. Jacobs also developed the dynamic simulation approach and led early feasibility studies. **Chad N. Weiler** is a Senior Professional Staff Optical Physicist in the Image Exploitation Group of the Asymmetric Operations Department. Dr. Weiler developed the atomic spectroscopy apparatus at the heart of the experimental effort and led the LIAD experiments. **Jeffrey P. Maranchi** is a Senior Professional Staff Materials Scientist and Group Supervisor in REDD. Dr. Maranchi oversaw all materials aspects of the ZEST program, ranging from device fabrication process planning to LIAD sample preparation and experimentation. **Chad R. Sprouse** is a Physicist with the Computa-

tional and Experimental Physics Group in REDD. Mr. Sprouse developed and implemented the novel tandem FDTD simulation technique used to analyze the ZEST approach. **Dennis G. Lucarelli** is a Senior Research Scientist and Section Supervisor in the Information Sciences Group in REDD. Dr. Lucarelli developed the quantum simulation approach and performed extensive numerical modeling of potential device performance. **Brian G. Rayburn** is an intern working with the ZEST team through the Oak Ridge Institute for Science and Education. Mr. Rayburn developed our fiber-tapering apparatus and assisted in all experimental activities. For further information about the work reported here, contact Bryan Jacobs. His e-mail address is [bryan.jacobs@jhuapl.edu](mailto:bryan.jacobs@jhuapl.edu).

The Johns Hopkins APL Technical Digest can be accessed electronically at [www.jhuapl.edu/techdigest](http://www.jhuapl.edu/techdigest).